



HAL
open science

On the influence of fabric layer shifts on the strain distributions in a multi-layer woven composite

Aurélien Doitrand, Christian Fagiano, Francois-Henri Leroy, Anne Mavel,
Martin Hirsekorn

► **To cite this version:**

Aurélien Doitrand, Christian Fagiano, Francois-Henri Leroy, Anne Mavel, Martin Hirsekorn. On the influence of fabric layer shifts on the strain distributions in a multi-layer woven composite. *Composite Structures*, 2016, 145, pp.15-25. 10.1016/j.compstruct.2016.02.054 . hal-01929284

HAL Id: hal-01929284

<https://hal.science/hal-01929284>

Submitted on 3 Nov 2022

HAL is a multi-disciplinary open access archive for the deposit and dissemination of scientific research documents, whether they are published or not. The documents may come from teaching and research institutions in France or abroad, or from public or private research centers.

L'archive ouverte pluridisciplinaire **HAL**, est destinée au dépôt et à la diffusion de documents scientifiques de niveau recherche, publiés ou non, émanant des établissements d'enseignement et de recherche français ou étrangers, des laboratoires publics ou privés.



Distributed under a Creative Commons Attribution - NonCommercial 4.0 International License

On the influence of fabric layer shifts on the strain distributions in a multi-layer woven composite

Aurélien Doitrand^{a,*}, Christian Fagiano^a, François-Henri Leroy^a, Anne Mavel^a,
Martin Hirsekorn^a

^a ONERA - The French Aerospace Lab - F-92322 Châtillon - France

Abstract

The influence of the relative shift between fabric layers on the local strain distributions at the mesoscopic scale of a four-layer plain weave glass fiber/epoxy matrix composite is studied through Finite Element (FE) modeling. The surface strain fields of several representative unit cells, consisting of compacted and nested plain weave layups with different layer shifts and the matrix complement, are compared to strain fields measured experimentally by digital image correlation. The layer shifts only have a small impact on the calculated homogenized macroscopic mechanical properties. However, the local strain fields are influenced significantly. Good quantitative agreement is obtained between the measured surface strain distributions and the numerical results if the layer shifts of the tested specimen are used in the FE model. The most frequently used models without layer shifts or with maximum nesting do not provide satisfactory surface strain distributions.

Keywords: Textile composites, Finite element analysis, Multiscale modeling

1. Introduction

Composite materials containing textile reinforcements are increasingly used for aeronautical and automotive lightweight applications. One of the advantages of woven com-

*Corresponding author, tel.: +33(0)146734658

Email adress: aurelien.doitrand@onera.fr (Aurélien Doitrand)

posites is the high flexibility of the fiber reinforcement, which can be directly shaped to the final form of a part, resulting in a reduction of assembly operations and of the number of weak points in a structure.

The reinforcement architecture of a woven composite has a strong influence on damage onset and propagation [1, 2]. For instance, different damage kinetics are observed for 2D [2, 3] and 3D woven composites [4]. Therefore, an experimental characterization of the damage mechanisms and of their influence on the material behavior is needed each time a different architecture is considered. The number of tests may be reduced using predictive models that take into account the reinforcement architecture, which is defined at the so-called meso-scale [5]. At this scale, the composite reinforcement is represented by two sets of interlaced yarns (warp and weft yarns) that are modeled as homogeneous materials embedded in the matrix.

At the meso-scale, the fiber reinforcement of woven composites is approximatively periodic, even if small variations are induced by (i) the weaving process, (ii) the handling of the fabric and (iii) the resin injection during composite manufacturing. Olave *et al.* [6] showed that the mechanical properties of the composites are not significantly influenced by these variations. Moreover, repeating damage patterns were observed along the edge of a woven composite specimen [7]. Therefore, perfect periodicity is often assumed to model woven composites, using a pattern representative of the whole material (called a representative unit cell, RUC), in order to reduce computational costs.

The shifts between the layers in a multi-layer woven composite may be controlled during the manufacturing process [1, 8]. However, this is a difficult operation and, in practice, random layer shifts are observed in most woven composites [6, 7, 9, 10]. These layer shifts are often neglected in meso-scale models. In several published papers, only one layer is modeled, assuming 3D periodic boundary conditions [11, 12, 13, 14, 15, 16].

Some authors [17, 18, 19] modeled all the fabric layers of multi-layer composites, but using in-phase layer stacks, thus not taking into account the layer shifts.

The influence of layer shifts on the mechanical behavior of woven composites was studied by several authors. Breiling *et al.* [20] showed that a variation of up to 32% on the ultimate strength of a carbon epoxy five-harness satin was obtained by varying the stacking configuration. Le Page *et al.* [21], solving a 2D problem, showed that the energy release rate of a cracked textile composite is strongly dependent on the stacking pattern. Ivanov *et al.* [22] found that the strain distributions were influenced by the layer shifts by comparing an in-phase and a shifted layup of an idealized geometry of a twill. The same authors showed in another paper [23] that damage onset was also strongly influenced. Daggumati *et al.* [24] studied the sensitivity of the surface strain distributions to different simplified stacking sequences (in phase, out-of phase and step stacking) of a 5-harness satin. A step stacking gave a better qualitative agreement compared to experimental data than in phase and out-of-phase stacks. However, the real layer shifts of the tested specimen, the fabric compaction and the nesting between the layers were not taken into account in the model.

In most models, the layer shifts are simplified for numerical convenience, thus not representing experimentally observed layups. Moreover, during the production process of a textile composite, the reinforcing fabric is usually compacted in order to increase the fiber volume fraction. As a consequence, the fabric layers nest into each other. The aim of this article is to evaluate numerically the influence of the layer shifts on the surface strain distributions in the case of a compacted and nested four-layer plain weave glass fiber/epoxy matrix composite. The results are compared to surface strain distributions measured experimentally by digital image correlation (DIC) on the specimen surfaces. The experimental tests are presented in section 2. Then the generation and meshing of five different RUCs is described in section 3. These RUCs contain compacted reinforce-

ments with (i) no shifts between the layers, (ii) shifts resulting in maximum nesting and (iii) the layer shifts determined experimentally on three specimens. Section 3 also includes the comparison between a geometry resulting from the numerical simulation of the compaction and a geometry extracted from a micro-computed tomography (μ -CT) observation of a specimen. In section 4, the homogenized properties and the surface strain distributions obtained numerically with the different RUCs are compared with the experimental observations.

2. Experimental analysis

The composite under investigation consists of four layers of a plain weave reinforcement of E-glass fibers embedded in Araldite LY564 epoxy resin. The thread count of the unbalanced plain fabric is $2.2 \text{ warps.cm}^{-1} \times 2 \text{ wefts.cm}^{-1}$. The fabric mass per unit area is $504 \pm 40 \text{ g.m}^{-2}$ and the mass density of the fibers is 2.54 g.cm^{-3} . The four layers composing the dry fabric were placed into a steel mold and compacted by tightening the screws that keep the mold closed. Due to the relative shift between adjacent layers, nesting occurs during compaction. After compaction and matrix injection, the mean fiber volume fraction in the material is 47%. Three rectangular specimens were tested under tensile loading in order to evaluate the in-plane elastic properties of the material and to measure the surface strain distributions using DIC. The orientation of the fiber reinforcement in the load direction of each specimen is respectively 0° (warp direction), 90° (weft direction) and 45° .

2.1. Reinforcement architecture

First, the specimen edges were observed using an optical microscope in order to determine the layer shifts of each specimen. These shifts are given in Table 1 for the three lower layers with respect to the top layer. The layer shifts that are modeled in most published works, *i.e.*, in-phase stacking resulting in no nesting and the shifts

resulting in maximum nesting, are also given. These five stacks are used in Section 3 for the generation of the Finite Element (FE) meshes of the composite RUCs.

Microscope observations on the edge of the specimens only provide a surface description of the reinforcement architecture. Therefore, the 0° specimen was scanned by means of an X-ray μ -CT, in order to obtain a full 3D description of the reinforcement architecture of one of the specimens (Figure 1a). A 3D geometrical representation of the reinforcement was generated by manually selecting each yarn outline on 20 2D tomography slices in warp and weft directions (Figure 1b). The resulting geometry is used in section 3 to validate the geometries obtained from the numerical modeling of the fabric compaction.

2.2. Surface strain distributions

The differences between the mechanical behavior of the stiff fibers and the compliant matrix result in heterogeneous strain distributions with strong gradients, especially around yarn crimp regions. Classical electrical resistance strain gages can thus not provide an adequate spatial resolution. Therefore, the local surface strains in woven composites are often measured using DIC. For example, Anzelotti *et al.* [25] and Nicoletto *et al.* [26] highlighted the weave-specific surface strain features of a specimen containing a single layer of twill-weave. Daggumati *et al.* [10] performed a local strain analysis on a 5-harness satin composite and matched the strain pattern with the reinforcement architecture and the locations of the resin rich areas. Koohbor *et al.* [27] showed that the in-plane surface strains have a strong influence on the failure mechanisms in several glass fiber and epoxy matrix specimens with different reinforcement orientations.

In this study, the surface strain distributions on the 3 specimens have been measured using 3D stereo-DIC. The displacements measured using 3D DIC are directly computed in the plane of the specimen, which is an advantage compared to 2D DIC where the

specimen must be perfectly aligned with the camera. In order to capture the surface strain distributions during the tensile tests, the specimen surfaces have been painted with a white spray followed by a black speckle pattern. Then, several images have been captured during the loading process. The local strains have been computed through the correlation between these images and an initial image of the unloaded specimen using the 'Limes-VIC3D' software [28]. The correlation step size was 3 pixels and the correlation subset size was 17 pixels. The strains obtained by derivation of the displacement fields are averaged over a 15 pixels window using a Gaussian filter, as explained in [28].

3. Finite element modeling of a Representative Unit Cell

3.1. Geometry generation

The dry reinforcement is usually compacted before adding the matrix in order to increase the fiber volume fraction and hence the mechanical properties of the composite. The compaction process leads to complex yarn shapes including local variations of both the section and the fiber volume fraction [6, 29]. If the fabric layer position is not precisely controlled during the manufacturing process, random shifts and nesting between the layers are obtained [30, 31]. Since the reinforcement architecture has a strong influence on the mechanical behavior of the composites, *e.g.*, on damage onset and propagation, it is essential to use a geometrical model of the reinforcement architecture that is as close as possible to that of the real specimen.

There are different methods to generate geometrical models of fabric reinforcements. First, the reinforcement architecture of a woven composite can be determined by post-treating μ -CT data [32]. The main advantage of this method is that the geometry exactly represents the real reinforcement, taking into account all the local variations of the architecture. However, since the material is not perfectly periodic, the choice

of a RUC and of the associated boundary conditions for FE analysis is not obvious. Geometrical models of fabric reinforcements can also be generated using automated tools that cover a large variety of weaving patterns [33, 34, 35, 36]. These models often neglect the deformation due to preforming, resulting in idealized geometries of the fabric and in much larger resin rich areas than observed experimentally. Therefore, in order to preserve the overall fiber volume fraction in the composite, the fiber volume fraction in the yarn must be set to unrealistically high values [22]. Geometries closer to the real composite can be obtained by modeling the preforming step of the dry fabric [7, 37, 38, 39]. The main objective of the compaction simulation is to obtain a realistic geometry of the reinforcement architecture including (i) a correct yarn volume fraction, (ii) a qualitative reproduction of the nesting between layers and (iii) an appropriate deformation of the yarn cross sections due to the neighboring yarns in contact. In this work, the simplified method described in [7], is used, which includes (i) a simplified mechanical behavior of the yarns, (ii) idealized yarn shapes in the non-compacted reinforcement and (iii) periodic boundary conditions on a single RUC, thus not accounting for the geometrical variability of the reinforcement architecture observed experimentally. This method is used to generate five geometries with different shifts between the fabric layers: (i) no shifts, (ii) shifts resulting in maximum nesting and (iii) the layer shifts measured on the three tested specimens (0° , 90° and 45°). The layer shifts of each RUC are summarized in table 1. Despite the simplified compaction modeling, the layer nestings in the generated RUCs agree well with optical microscope observations on the edges of the three specimens. The microscope images are shown together with the geometries in Figure 2.

3.2. Comparison with μ -CT observations

The 3 RUC geometries corresponding to the tested specimens have been generated using the layer shifts measured on the edges of the specimens. It can be seen from Figure

2 that the reinforcement geometry obtained from the compaction simulation using the layer shifts of the 0° specimen qualitatively agrees well with the μ -CT observation. For a quantitative comparison, we evaluated (i) the yarn (warp and weft) wavelength, (ii) the spacing between the yarn middle lines of each layer, (iii) the yarn volume fraction and (iv) the yarn mean cross section area. The averages of each of these parameters taken separately in warp and weft direction are summarized in Table 2. The differences between the modeled geometry and the μ -CT observation are small ($< 3.5\%$). Therefore, we conclude that the simplified compaction modeling yields geometries that are representative of the geometric features of a compacted and nested fiber reinforcement.

3.3. Mesh generation of the RUCs

Meso-scale FE analysis of woven composites requires the generation of a mesh of the RUC containing the deformed reinforcement and the matrix complement. A method that is widely used, due to its simplicity, is voxel meshing [11, 12, 40, 41, 42, 43, 44]. This method allows for a correct prediction of the elastic properties of undamaged materials, provided that a converged mesh is used. However, several limitations arise when predicting damage onset [7] since the yarn surfaces are not correctly represented by the element faces. The generation of consistent FE meshes with element faces that follow accurately the yarn surfaces is complex [38], especially in the zones where yarns are in contact. Therefore, a matrix layer is often inserted between the yarns [5, 15, 18, 45], which considerably simplifies the meshing procedure since each yarn can be meshed separately. If the layer is thin, very small elements are needed to avoid bad mesh quality, and if it is thick, a lower yarn volume fraction is obtained in the RUC. Therefore, the method of Grail [38], which allows the generation of consistent meshes of 2D woven composite RUCs, is used in this work to generate the FE meshes of the geometries obtained by compaction simulation. The meshes that are conformal at the contact zones between the yarns and between matrix and yarns, are composed of

quadratic tetrahedral elements to ensure an accurate modeling of the stress and strain gradients.

4. Comparison between numerical and experimental results

4.1. Comparison of macroscopic homogenized properties

The macroscopic elastic properties of the studied material are calculated by means of meso-macro homogenization on the five meshed RUCs previously presented. The matrix is supposed to be linear elastic. The mechanical properties of the matrix given by the manufacturer are: Young's modulus $E_m = 3.2$ GPa and Poisson's ratio $\nu_m = 0.35$. The yarn behavior is obtained by micro-meso homogenization, as in Ref. [15], using $E_f = 73.6$ GPa [46] and $\nu_f = 0.3$ for the fibers. The fiber volume fraction in the yarns is chosen such that the overall fiber volume fraction in the RUC is similar to the fiber volume fraction in the composite, *i.e.*, 47%. Since the layer shifts are different for the five studied RUCs, the compaction process leads to different layer nestings with more or less deformed yarns. Therefore, yarn volume fractions are not the same for each RUC. As a consequence, the fiber volume fraction in the yarns has been adapted for each RUC to reach an overall fiber volume fraction of 47%. Moreover, the ratio between warp and weft volume fractions after the compaction simulation is not exactly equal to the ratio between the respective thread counts in the fabric. Therefore, different fiber volume fractions are used for warp and weft yarns such that the ratio between the fiber volumes in warp and weft yarns corresponds to that of the real material. The transverse isotropic elastic yarn properties calculated for each RUC are summarized in Table 3. The local orientation of the yarn material is calculated separately at each integration point through orthogonal projection of its position on the central line of the yarn. The transverse isotropy axis of the yarn material, *i.e.*, the fiber direction, is determined as the tangent to the central line at the projected point. Periodic boundary conditions are

applied in the fabric plane directions of the RUC, whereas the top and bottom surfaces are left free in order to correctly represent the boundary conditions of the composite specimens in a tensile test. A uniaxial stress state in warp (respectively weft) direction (parallel to the Y-axis (respectively X-axis)) is applied to the RUC in order to model a tensile test on the 0° (respectively 90°) specimen. It is given by $\underline{\underline{\sigma}}$ in equation 1. In the 45° specimen, the warp and weft directions are rotated by 45° with respect to the loading direction. Therefore, the stress tensor $\underline{\underline{\sigma}}_R$ is applied to the RUC with the directions of periodicity (directions of the warp and weft yarns) parallel to the X and Y axes. It is obtained from $\underline{\underline{\sigma}}$ by a rotation of 45° around the Z-axis:

$$\underline{\underline{\sigma}}_R = P \cdot \underline{\underline{\sigma}} \cdot P^T = \begin{pmatrix} \frac{\sigma}{2} & -\frac{\sigma}{2} & 0 \\ -\frac{\sigma}{2} & \frac{\sigma}{2} & 0 \\ 0 & 0 & 0 \end{pmatrix} \text{ with } P = \begin{pmatrix} \frac{\sqrt{2}}{2} & -\frac{\sqrt{2}}{2} & 0 \\ \frac{\sqrt{2}}{2} & \frac{\sqrt{2}}{2} & 0 \\ 0 & 0 & 1 \end{pmatrix} \text{ and } \underline{\underline{\sigma}} = \begin{pmatrix} 0 & 0 & 0 \\ 0 & \sigma & 0 \\ 0 & 0 & 0 \end{pmatrix} \quad (1)$$

The measured elastic properties and those obtained through homogenization on the 5 RUCs are compared in Table 4. The influence of the layer shifts on the homogenized elastic properties is small.

4.2. Comparison of surface strain distributions

The strain distributions measured on the three studied specimens and the surface strain distributions obtained numerically are shown in Figure 3 for the 0° specimen, in Figure 4 for the 90° specimen and in Figure 5 for the 45° specimen. ϵ_{yy} is the longitudinal and ϵ_{xx} the transverse strain component under tensile load in the y-direction. The numerically calculated strain distributions are averaged using a Gaussian filter over the same window size as in the post treatment of the DIC data (see Section 2). During the tests of the 45° and the 90° specimens, an extensometer was fixed to the specimen. Therefore the measured strain distributions are separated in three parts since the

speckle was hidden by the extensometer in two areas.

The surface strain fields obtained from the RUCs without shifts and with maximum nesting of the reinforcement differ significantly from the strain patterns observed experimentally. These types of RUC, which are mostly used in published articles about meso-scale modeling of woven composites, do not provide satisfactory surface strain distributions. Fewer differences are observed between the results obtained from the three RUCs with layer shifts determined experimentally on the specimen edges. The best qualitative agreement between the experimental and numerically calculated strain distributions is obtained if the layer shifts corresponding to the considered specimen are used. A quantitative comparison of the strain fields measured experimentally on the three specimens and those computed with the corresponding RUC with the same layer shifts is shown in Figures 6-8. The longitudinal (Figure 6-8a) and transverse (Figure 6-8b) strain evolutions are calculated along several lines on the specimen surface (Figure 6-8c and d), two consecutive lines being separated by one RUC length. The variations between the experimental strains along different lines can be explained by small variations of the reinforcement architecture induced during the manufacturing process. Since the RUC is periodic, the numerically calculated strain evolutions are repeated periodically for the comparison with the experimental data (Figure 6-8c and d). The strains on the surface of the 45° specimen are shown based on the coordinates of the experimental setup (tension parallel to the Y-axis), *i.e.*, the strain fields obtained from the FE calculations are rotated back by 45° (the opposite of the rotation described in Eq. 1). Since the fabric is slightly unbalanced (the RUC is not exactly a square in the X-Y plane), the directions of periodicity are not exactly parallel to the X and Y axes in the experimental setup. The strain profiles shown in Figure 8 are taken along these directions of periodicity. The measured strains agree well with the calculated strains along the corresponding line on the respective RUC.

5. Conclusion

The three RUCs generated by means of the simplified numerical simulation of the fabric compaction described in [6], using the layer shifts observed on the specimen edges, provide a satisfactory model of the composite specimens with realistic fiber volume fractions and yarn shapes, including nesting between the fabric layers. This has been shown by comparison with 2D optical microscope images of the specimen edges and in 3D by comparison of the whole RUC of the 0° specimen with a μ -CT scan.

The differences between the homogenized elastic properties calculated using five different RUCs with different relative layer shifts, including those of the three tested specimens and the two extreme cases without layer shifts and with shifts maximizing the nesting between the layers, are relatively small. The calculated elastic properties are in good agreement with the experimental values. Therefore, for the prediction of the homogenized elastic properties, arbitrary layer shifts may be used, including simplified models without shifts, as in [18, 19, 24].

A significant influence of the layer shifts on the surface strain distributions has been observed. In particular, the idealized cases of in-phase stacking and maximum nesting yield strain fields that differ considerably from those observed experimentally by DIC. If random layer shifts are used, the differences decrease significantly. The RUC with the layer shifts determined on the edges of the corresponding specimen yields the best qualitative (location of the extrema) and quantitative (absolute values) agreement of the surface strain fields with the experimental observations.

Since damage onset in the composite depends on local stress or strain concentrations, the RUCs with the experimentally determined layer shifts seem appropriate to model damage onset and propagation at the mesoscopic scale. Simplified layouts that do not take into account the shifts and the nesting between the fabric layers may lead to erroneous predictions of damage onset locations and propagation.

References

- [1] De Carvalho NV, Pinho ST, Robinson P. An experimental study of failure initiation and propagation in 2D woven composites under compression. *Composites Science and Technology* 2011;71,1316-25.
- [2] Tang X, Whitcomb J. Progressive failure behaviors of 2D woven composites. *Journal of Composite Materials* 2003;37:1239-59.
- [3] Osada T, Nakai A, Hamada H. Initial fracture behavior of satin woven fabric composites. *Composite Structures* 2003;61:333-9.
- [4] Dai S, Cunningham PR, Marshall S, Silva C. Influence of fibre architecture on the tensile, compressive and flexural behaviour of 3D woven composites. *Composites Part A* 2015;69:195-207.
- [5] Lomov SV, Ivanov DS, Verpoest I, Zako M, Kurashiki T, Nakai H, Hirosawa S. Meso-FE modelling of textile composites: Road map, data flow and algorithms. *Composites Science and Technology* 2007;67(9):1870-91.
- [6] Olave M, Vanaerschot A, Lomov S, Vandepitte D. Internal geometry variability of two woven composites and related variability of the stiffness. *Polymer Composites* 2012;33(8):1335-50.
- [7] Doitrand A, Fagiano C, Chiaruttini V, Leroy FH, Mavel A, Hirsekorn M. Experimental characterization and numerical modeling of damage at the mesoscopic scale of woven polymer matrix composites under quasi-static tensile loading. *Composites Science and Technology* 2015;119:1-11.
- [8] Hale RD, Villa M. Influence of opposing wave nesting in compression-loaded. *Journal of Composite Materials* 2003;37:1149-66.
- [9] John S, Herszberg I, Coman F. Longitudinal and transverse damage taxonomy in woven composite components. *Composites Part B* 2001;32(8):659-68.
- [10] Daggumati S, Voet E, Van Paepegem W, Degrieck J, Xu J, Lomov SV, Verpoest

- I. Local strain in a 5-harness satin weave composite under static tension Part I Experimental analysis. *Composites Science and Technology* 2011;71,1171-79;
- [11] De Carvalho NV, Pinho ST, Robinson P. Reducing the domain in the mechanical analysis of periodic structures, with application to woven composites. *Composites Science and Technology* 2011;71(7):969-79.
- [12] Kim HJ, Swan CC. Voxel-based meshing and unit-cell analysis of textile composites. *International Journal for Numerical Methods in Engineering* 2003;56:977-1006.
- [13] Zako M, Uetsuji Y, Kurashiki T. Finite element analysis of damaged woven fabric composite materials. *Composites Science and Technology* 2003;63:507-16.
- [14] Ivanov DS, Baudry F, Van Den Broucke B, Lomov SV, Xie H, Verpoest I. Failure analysis of triaxial braided composite. *Composites Science and Technology* 2009;69(9):1372-80.
- [15] Melro P, Camanho P, Andrade Pires FM, Pinho ST. Numerical simulation of the non-linear deformation of 5-harness satin weaves. *Computational Materials Science* 2012;61(0):116-26.
- [16] Lomov SV, Ivanov DS, Verpoest I, Zako M, Kurashiki T, Nakai H, Molimard J, Vautrin A. Full-field strain measurements for validation of meso-FE analysis of textile composites. *Composites Part A* 2008;39:1218-31.
- [17] Ivanov DS, Lomov SV, Ivanov SG, Verpoest I. Stress distribution in outer and inner plies of textile laminates and novel boundary conditions for unit cell analysis. *Composites Part A* 2010.41:571:80.
- [18] De Carvalho NV, Pinho ST, Robinson P. Numerical modelling of woven composites: biaxial loading. *Composites Part A* 2012;43(8):1326-37.
- [19] Römelt P, Cunningham PR. A multi-scale finite element approach for modelling damage progression in woven composite structures. *Composite Structures* 2012;94(3):977-86.

- [20] Breiling K, Adams DO. Effects of layer nesting on compression-loaded 2-d woven textile composites. *Journal of Composite Materials* 1996;30:1710-28.
- [21] Le Page BH, Guild FJ, Ogin SL, Smith PA. Finite element simulation of woven fabric composites. *Composites Part A* 2004;35:861-72.
- [22] Ivanov D, Ivanov S, Lomov SV, Verpoest I. Strain mapping analysis of textile composites. *Optics and Lasers in Engineering* 2009;47:360-70.
- [23] Ivanov DS, Ivanov SG, Lomov SV, Verpoest I. Unit cell modelling of textile laminates with arbitrary inter-ply shifts. *Composites Science and Technology* 2011;72:14-20.
- [24] Daggumati S, Van Paepegem W, Degrieck J, Praet T, Verhegghe B, Xu J, Lomov SV, Verpoest I. Local strain in a 5-harness satin weave composite under static tension Part II Meso-FE analysis. *Composites Science and Technology* 2011;71,1217-24.
- [25] Anzelotti G, Nicoletto G, Riva E. Mesomechanic strain analysis of twill-weave composite lamina under unidirectional in-plane tension. *Composites Part A* 2008;39:1294-301.
- [26] Nicoletto G, Anzelotti G, Riva E. Mesoscopic strain fields in woven composites Experiments vs. finite element modeling. *Optics and Lasers in Engineering* 2009;47:325-59.
- [27] Koohbor B, Ravindran S, Kidane A. Meso-Scale Strain Localization and Failure Response of an Orthotropic Woven glass fibre reinforced composite. *Composites Part B* 2015;78:308-18.
- [28] VIC-3D 2010 Reference Manual. <http://www.correlatedsolutions.com/installs/>.
- [29] Karahan M, Lomov SV, Bogdanovich AE, Mungalov D, Verpoest I. Internal geometry evaluation of non-crimp 3D orthogonal woven carbon fabric composite. *Composites Part A* 2010;41:1301-11.
- [30] Chen B, Lang EJ, Chou TW. Experimental and theoretical studies of fabric

- compaction behavior in resin transfer molding. *Materials Science and Engineering* 2001;317:188-96.
- [31] Lomov SV, Verpoest I, Peeters T, Roose D, Zako M. Nesting in textile laminates: geometrical modelling of the laminate. *Composites Science and Technology* 2003;63:993-1007.
- [32] Naouar N, Vidal-sallé E, Schneider J, Maire E, Boisse P. Meso-scale FE analyses of textile composite reinforcement deformation based on X-ray computed tomography. *Composite Structures* 2014;116:165-76.
- [33] Couegnat G. Approche multiéchelle du comportement mécanique de matériaux composites à renfort tissé. Ph.D. thesis, Université de Bordeaux 1, 2008. <https://tel.archives-ouvertes.fr/tel-00403885/>
- [34] Verpoest I, Lomov SV. Virtual textile composites software WiseTex: Integration with micro-mechanical, permeability and structural analysis. *Composites Science and Technology* 2005;65:2563-74.
- [35] Sherburn M. Geometric and mechanical modelling of textiles. Ph.D. thesis, The University of Nottingham, 2007. <http://eprints.nottingham.ac.uk/10303/>
- [36] Adanur S, Liao T. 3D modeling of textile composite preforms. *Composites Part B* 1998;29:787-93.
- [37] Nguyen QT, Vidal-Sallé E, Boisse P, Park CH, Saouab A, Breard J, Hivet G. Mesoscopic scale analyses of textile composite reinforcement compaction. *Composites Part B* 2012;44(1):231-41.
- [38] Grail G, Hirsekorn M, Wendling A, Hivet G, Hambli R. Consistent Finite Element mesh generation for meso-scale modeling of textile composites with preformed and compacted reinforcements. *Composites Part A* 2013;55:143-51.
- [39] Lin H, Sherburn M, Crookston J, Long A, Clifford M, Jones I. Finite element modelling of fabric compression. *Modeling and Simulation in Materials Science and*

- Engineering 2008;16(3)035010(16pp).
- [40] Zeng X, Brown LP, Endruweit A, Matveev M, Long AC. Geometrical modelling of 3D woven reinforcements for polymer composites: Prediction of fabric permeability and composite mechanical properties. *Composites Part A* 2014;56:150-60.
 - [41] Potter E, Pinho ST, Robinson P, Iannucci L, McMillan AJ. Mesh generation and geometrical modeling of 3D woven composites with variable tow cross-sections. *Computational Materials Science* 2012;51(1):103-11.
 - [42] Koumpias AS, Tserpes KI, Pantelakis S. Progressive damage modelling of 3D fully interlaced woven composite materials. *Fatigue and Fracture of Engineering Materials and Structures* 2014;37(7):696-706.
 - [43] Doitrand A, Fagiano C, Irisarri FX, Hirsekorn M. Comparison between voxel and consistent meso-scale models of woven composites. *Composites Part A* 2015;73:143-54.
 - [44] Green SD, Matveev MY, Long AC, Ivanov D, Hallett SR. Mechanical modelling of 3D woven composites considering realistic unit cell geometry. *Composite Structures* 2014;118:284-93.
 - [45] Stig F, Hallström S. A modelling framework for composites containing 3D reinforcement. *Composite Structures* 2012;94(9):2895-901.
 - [46] Rocher JE, Allaoui S, Hivet G, Gillibert J, Blond E. Experimental characterization and modeling of GF/PP commingled yarns tensile behavior. *Journal of Composite Materials* 2015;49(21):2609-24.

Figure captions

Fig. 1 - Geometry of the reinforcement of the 0° specimen (one RUC) obtained (a) from the μ -CT scan and (b) from compaction modeling.

Fig. 2 - Comparison between microscope observations (top) of the edge of the (a) 90° , (b) 0° and (c) 45° specimens and the edge of the corresponding RUC (bottom) in weft (left) and warp (right) direction. (d) RUC with maximum nesting and (e) RUC without nesting.

Fig. 3 - Longitudinal (ϵ_{yy} , left) and transverse (ϵ_{xx} , right) strain distributions under tensile loading in the y-direction obtained using (a) the RUC determined from the 0° specimen, (b) the RUC determined from the 90° specimen, (c) the RUC without nesting, (d) the RUC determined from the 45° specimen, (e) the RUC with maximum nesting, and (f) observed by DIC on the 0° specimen.

Fig. 4 - Longitudinal (ϵ_{yy} , left) and transverse (ϵ_{xx} , right) strain distributions under tensile loading in the y-direction obtained using (a) the RUC determined from the 0° specimen, (b) the RUC determined from the 90° specimen, (c) the RUC without nesting, (d) the RUC determined from the 45° specimen, (e) the RUC with maximum nesting, and (f) observed by DIC on the 90° specimen.

Fig. 5 - Longitudinal (ϵ_{yy} , left) and transverse (ϵ_{xx} , right) strain distributions under tensile loading in the y-direction obtained using (a) the RUC determined from the 0° specimen, (b) the RUC determined from the 90° specimen, (c) the RUC without nesting, (d) the RUC determined from the 45° specimen, (e) the RUC with maximum nesting, and (f) observed by DIC on the 45° specimen.

Fig. 6 - Longitudinal (ϵ_{yy} , left) and transverse (ϵ_{xx} , right) strain distributions under tensile loading in the y-direction (a) observed experimentally for the 0° specimen and (b) calculated numerically using the corresponding RUC. Quantitative comparison

along several lines of (c) longitudinal and (d) transverse experimental (lines drawn in (a)) and numerical (line drawn in (b)) strain profiles.

Fig. 7 - Longitudinal (ϵ_{yy} , left) and transverse (ϵ_{xx} , right) strain distributions under tensile loading in the y-direction (a) observed experimentally for the 90° specimen and (b) calculated numerically using the corresponding RUC. Quantitative comparison along several lines of (c) longitudinal and (d) transverse experimental (lines drawn in (a)) and numerical (line drawn in (b)) strain profiles.

Fig. 8 - Longitudinal (ϵ_{yy} , left) and transverse (ϵ_{xx} , right) strain distributions under tensile loading in the y-direction (a) observed experimentally for the 45° specimen and (b) calculated numerically using the corresponding RUC. Quantitative comparison along several lines of (c) longitudinal and (d) transverse experimental (lines drawn in (a)) and numerical (line drawn in (b)) strain profiles.

Shifts [mm]	layer 1 (top layer)	layer 2	layer 3	layer 4
0°-specimen	Warp direction	-0.61	-0.59	0.43
	Weft direction	-0.30	3.43	2.93
90°-specimen	Warp direction	1.32	2.50	-3.56
	Weft direction	1.71	3.24	4.09
45°-specimen	Warp direction	-2.57	0.58	-2.31
	Weft direction	-0.63	0.29	0.59
No nesting	Warp direction	0	0	0
	Weft direction	0	0	0
Nesting max	Warp direction	2.27	0	2.27
	Weft direction	2.50	0	2.50

Table 1: Layer shifts in warp and weft directions with respect to the top layer (the layers are numbered from top to bottom).

Property	Yarn type	Specimen	RUC-0°	Difference
Yarn wavelength [mm]	Warps	9.17	9.1	1.9%
	Wefts	10.3	10.01	2.8%
Spacing between middle lines [mm]	Warps	5.01	5.02	0.2%
	Wefts	4.57	4.55	0.44%
Volume fraction	Warps	40.4%	42.4%	2.0%
	Wefts	46.3%	46.2%	0.1%
Mean cross section area [mm ²]	Warps	0.89	0.88	1.1%
	Wefts	0.86	0.89	3.5%

Table 2: Comparison between geometrical parameters obtained from a μ -CT scan and from simulation of dry fabric compaction with layer shifts determined on the specimen edges.

RUC	Yarn type	Volume fraction (%)	E_l [GPa]	E_t [GPa]	ν_{lt}	ν_{tt}	G_{lt} [GPa]
RUC-0°	Warps	41.1	41.5	9.7	0.32	0.43	7.1
	Wefts	44.9	41.8	9.8	0.32	0.43	7.2
RUC-90°	Warps	37.3	45.5	11.3	0.32	0.41	8.2
	Wefts	40.8	45.7	11.4	0.32	0.41	8.3
RUC-45°	Warps	37.5	44.3	11.1	0.32	0.41	8.2
	Wefts	40.3	45.2	11.6	0.32	0.41	8.5
No nesting	Warps	37.5	45.2	11.2	0.32	0.41	8.2
	Wefts	42.9	43.6	10.5	0.32	0.42	7.7
Nesting max	Warps	44.3	38.7	8.8	0.32	0.44	6.5
	Wefts	48.6	38.8	8.8	0.32	0.44	6.5

Table 3: Homogenized elastic properties of the warp and weft yarns used in the FE simulations of the five RUCs.

Properties	Experimental	RUC-0°	RUC-90°	RUC-45°	no nesting	nesting max
E_{0° [GPa]	20.3 ± 0.3	21.2	21.7	20.4	21.0	20.7
ν_{0°	0.126 ± 0.009	0.132	0.129	0.138	0.142	0.133
E_{90° [GPa]	22.5 ± 0.5	21.5	22.9	21.5	22.6	21.9
ν_{90°	0.147 ± 0.007	0.134	0.136	0.146	0.153	0.141
E_{45° [GPa]	11.2 ± 0.7	10.04	10.66	10.43	10.20	9.87
ν_{45°	0.517 ± 0.02	0.59	0.59	0.57	0.60	0.60

Table 4: Macroscopic mechanical properties measured experimentally and calculated by means of FE periodic homogenization using several RUCs with different layer shifts.

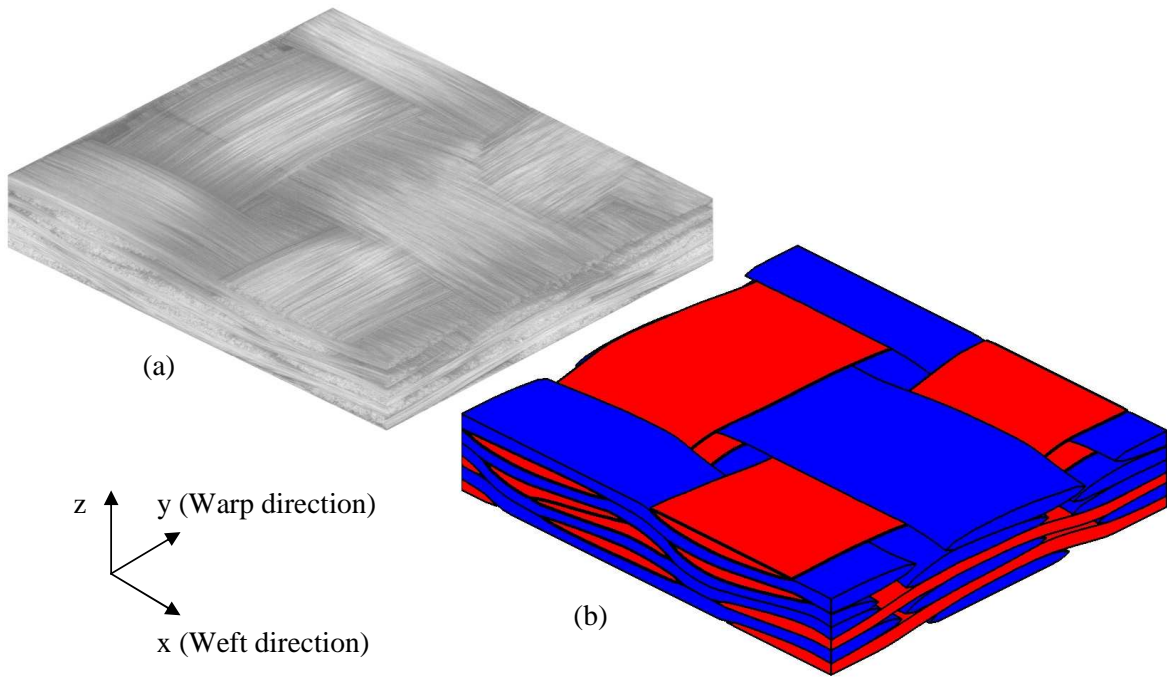


Figure 1:

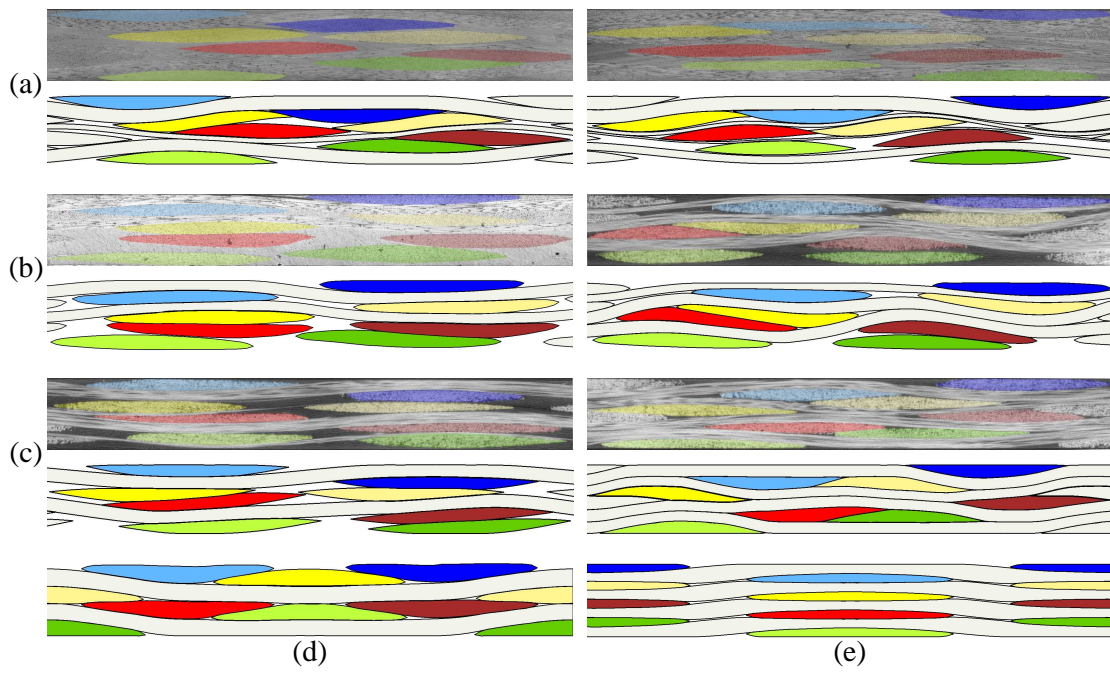


Figure 2:

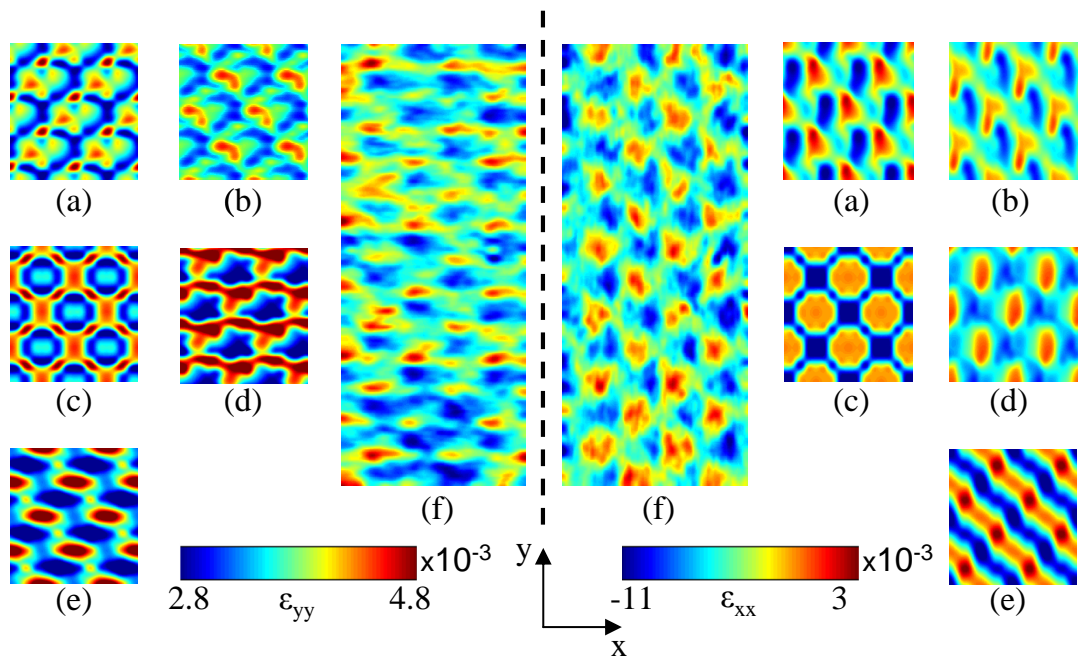


Figure 3:

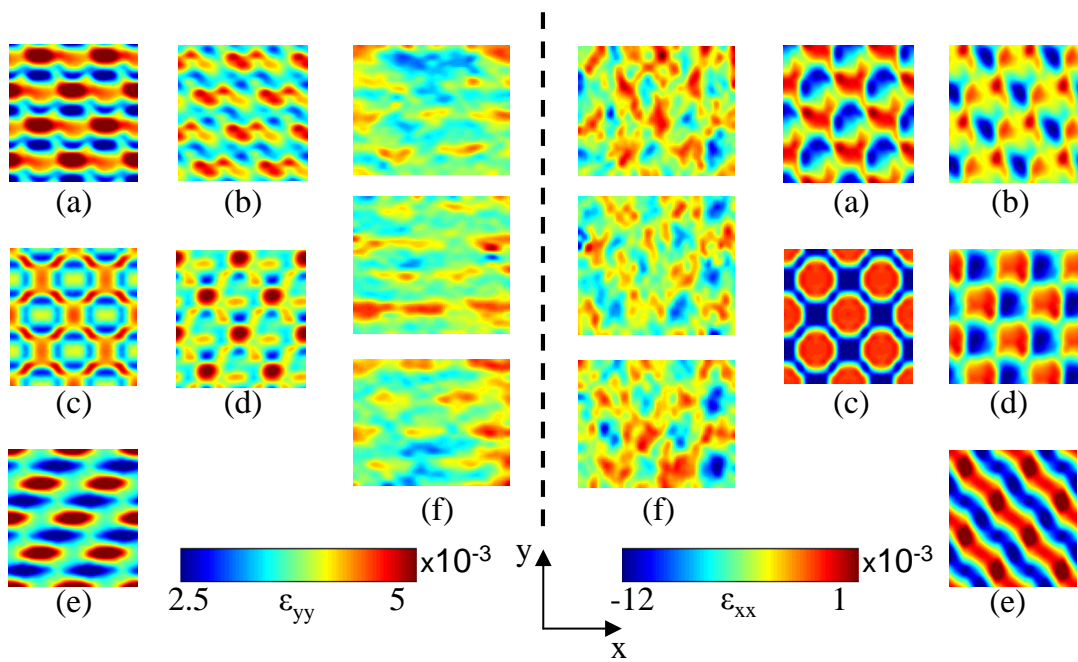


Figure 4:

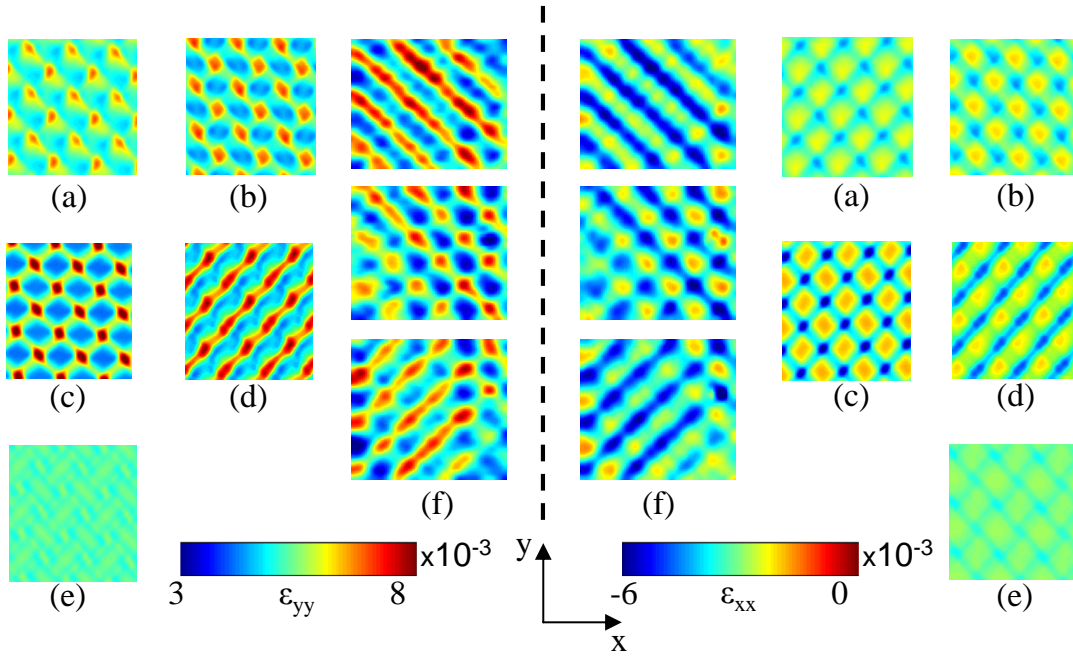


Figure 5:

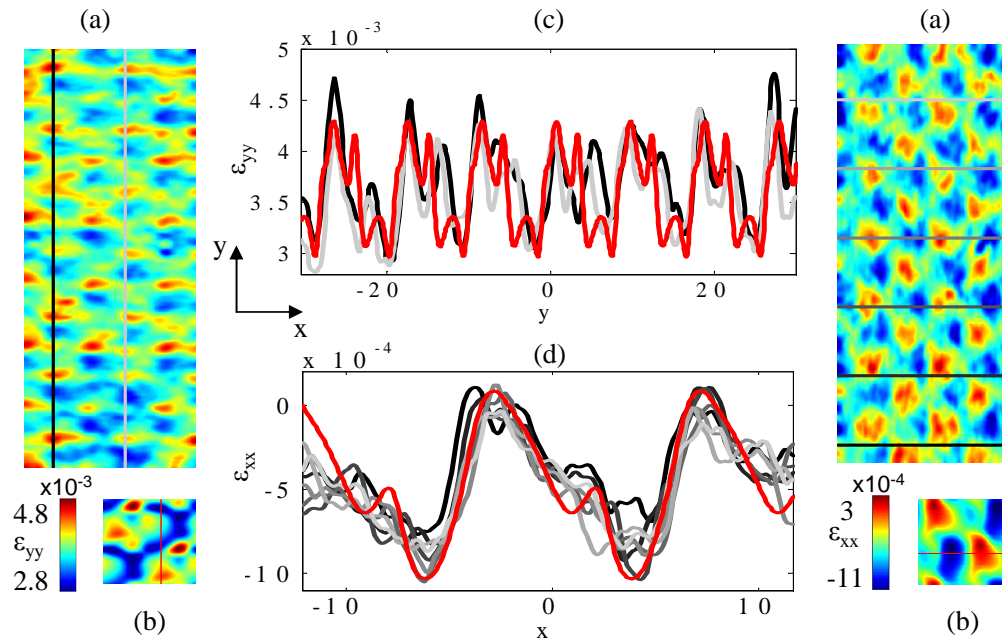


Figure 6:

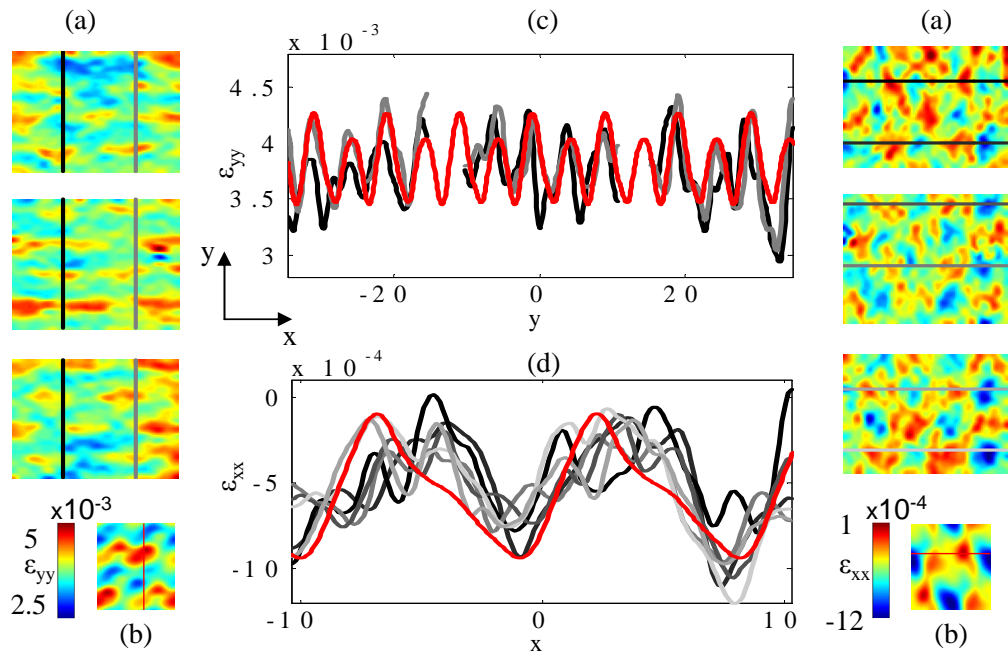


Figure 7:

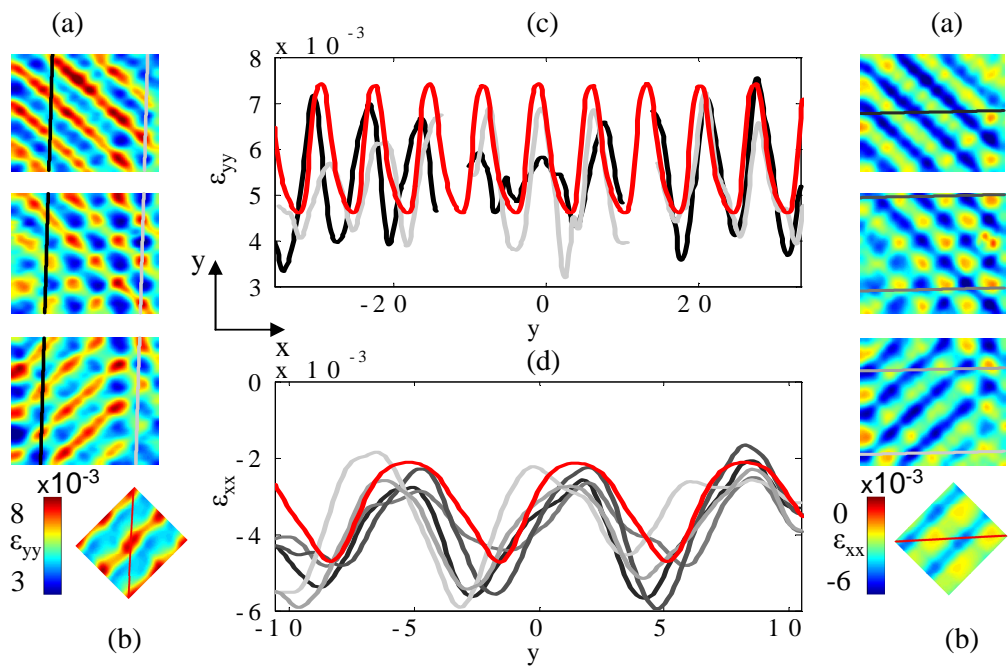


Figure 8: